

Axial load resistance of a novel UHPFRC grouted SHS tube sleeve connection: experimental, numerical and theoretical approaches

Zhenyu HUANG¹, Wei ZHANG^{2*}, Shiyong FAN³, Lili SUI⁴, Jianqiao YE⁵

¹ Guangdong Provincial Key Laboratory of Durability for Marine Civil Engineering, Shenzhen University. A412, School of Civil Engineering, Shenzhen University, Shenzhen, China 518060. Email:

huangzhenyu@szu.edu.cn

² Guangdong Provincial Key Laboratory of Durability for Marine Civil Engineering, Shenzhen University. L1-1408, Shenzhen University, Shenzhen, China 518060. Email: zhangwdnv@gmail.com

³ Guangdong Provincial Key Laboratory of Durability for Marine Civil Engineering, Shenzhen University. L1-1508, Shenzhen University, Shenzhen, China 518060. Email: fsy972632164@126.com

⁴ Guangdong Provincial Key Laboratory of Durability for Marine Civil Engineering, Shenzhen University. A503, School of Civil Engineering, Shenzhen University, Shenzhen, China 518060. Email: suill@szu.edu.cn

⁵ Department of Engineering, Lancaster University. B09, B-Floor, Engineering Building, Lancaster University, Lancaster LA1 4YR, UK. Email: j.ye2@lancaster.ac.uk

Abstract

This study conducts experimental, numerical and theoretical analyses on the axial load resistance of a novel ultra-high performance fiber reinforced concrete (UHPFRC) grouted square hollow section (SHS) tube sleeve connection. The experimental study tests ten full-scale specimens with varying shear key spacings, grout thicknesses, grout lengths and volume proportions of steel fiber in the UHPFRC. Two types of failure modes are observed: (1) for the connection with high strength of the grouted part, the failure mode is fracture of the inner tube; (2) for the connection with lower strength of the grouted part, the failure mode is grout shear crushing with significant bond-slip between grout and steel tube. To further understand the load transfer mechanism of the connection, an advanced 3D nonlinear FE model is built to simulate the axial load-displacement behavior, state of stress and strain, as well as crack development of the grout. Based on the test and FE results, a new theoretical model is derived to predict the axial load resistance of the connection. The proposed model has considered the effect of section shape and material parameters, and is applicable to UHPFRC grouted SHS tube sleeve connection with different corner radii. The validations against the test results show that the new model can provide reasonably effective and accurate predictions to the axial load resistance of the novel grouted sleeve connection subjected to tension.

Keywords: sleeve connection, UHPFRC, axial load resistance, shear key, friction and adhesion

32 **1. Introduction**

33 Modular construction, by which modules are prefabricated off-site and assembled on-site, has become
34 a popular option in construction industry due to its higher efficiency and productivity [1,2], better
35 quality and safety [3,4], as well as lesser labor intensive and pollution [5]. Depending on the degree of
36 off-site manufacturing, modular unit may vary from simple stick frame systems, such as pre-cast
37 concrete or prefabricated bathroom pods, to fully prefabricated prefinished volumetric constructed
38 (PPVC) module [6]. A PPVC module is completed with internal finishes, fixtures and fittings in an off-
39 site fabrication facility, before it is delivered and installed on-site, thus offers the highest prefabrication
40 rate [7]. One of the most critical issues affecting the integrity and safety of modular buildings is the
41 connections between the PPVC modules [8].

42 PPVC modules are normally connected externally for minimization of interior decoration on-site
43 [9]. According to joint locations, connections are classified as corner, perimeter and interior connections,
44 respectively. Bolted connections are the most-commonly used connections, including beam-beam
45 connections, column-column connections and beam-column connections. Extensive research has been
46 conducted in this field. Liu et al. [10] investigated the ultimate load resistance of a bolted-flange
47 column-column connection under combined compression, bending and shearing. Load-transfer
48 mechanism was studied and load resistance equations were proposed following the yield line theory
49 and T-stub analogy. Chen et al. [11] designed a novel beam-beam bolted connection that provides easy
50 access interior module connections, and experimentally investigated its static and hysteretic behaviors.
51 The ultimate strength and energy dissipation ability of the interior connection were found to be sensitive
52 to the bending stiffness of each unit joints and their relative stiffness. Torbaghan et al. [12] investigated
53 the performance of a simple and efficient moment connection for pre-fabricated steel structures

54 subjected to cyclic loading. Both experimental tests and FE simulations were performed on connections
55 of beams, columns, plates and stiffeners of varying thicknesses. The connections exhibit excellent
56 performance under cyclic loading. Although bolted connections are widely used, there are still some
57 critical issues requiring attention. Firstly, the accumulation of geometric and positioning deviations may
58 easily cause alignment issues especially for high-rise modular buildings [13-15]. Secondly, corrosion is
59 a critical problem for bolted connections exposed to humid weather environment [16]. Thirdly,
60 extensive usage of bolted connections may reduce productivity of modular construction and cause
61 collision during modular assembling [17, 18].

62 To overcome these issues, a shear key-grouted column connection of square hollow section (SHS)
63 was developed, which connects the upper and lower columns by filling the gap in the overlapped zone
64 of the connection with grout [19]. The idea of the SHS column connection originates from the CHS
65 column connection. The difference is that the CHS column connection consists of circular hollow
66 section tubes, and is widely used in offshore structures due to the excellent streamline, such as offshore
67 pile foundations and the transition parts of wind turbine towers, etc. In contrast, the SHS column
68 connection can be applied in modular construction industry as it is easy for installation, arrangement
69 and standardization. Extensive studies have been conducted to investigate failure modes and load
70 resistances of CHS pile-to-sleeve connections [20-22]. Axial load resistance of a grouted connection is
71 attributed to the bond strength due to friction and adhesion between grout and steel tube, and the
72 mechanical interlock provided by shear keys [23-25]. Many full-scale [26-27] or large-scale [28-30]
73 experiments have been conducted to evaluate load resistance of pile-to-sleeve connections. Krahl and
74 Karsan [31] were the first to analyze load transfer mechanism of shear key-grouted pile-to-sleeve
75 connections, and proposed an analytical equation for axial load resistance based on the compression

76 strut model. Lee et al. [32] experimentally and numerically investigated the axial load resistance of
77 high-strength grouted connections and studied the influence of loading eccentricity. The comparisons
78 show that the load resistance under concentric loading is very close to that under eccentric loading.
79 Chen et al. [33] conducted a series of parametric analyses based on an established FE model and
80 concluded that increasing radial stiffness and shear key height-to-spacing ratio could effectively
81 increase axial load resistance of pile-to-sleeve connections. Lotsberg [34] studied the structural
82 mechanics of grouted connections in monopile wind turbine structures when they were subjected to not
83 only axial force but also severe dynamic moment. A design methodology was proposed for ultimate
84 limit state and fatigue limit state designs.

85 Existing design codes, including DNV 2014 [35], NORSORK 2012 [36], API 2007 [37], ISO 2007
86 [38], have recommended various equations for calculating axial load resistance of pile-to-sleeve
87 connections. However, these equations cannot be directly applied to SHS column connections, as the
88 confinement effect on the grout is quite different. Sui et al. [19] investigated the load transfer
89 mechanisms of a grouted prefabricated SHS column connection under axial compression and tension.
90 The investigation concludes that for a connection under axial compression, load is transferred from the
91 upper outer tube to the lower outer tube. The load resistance is dominated by the geometric sizes and
92 material properties of the outer tubes. For a connections under axial tension, load is transferred from
93 the upper outer tube to the inner tube through the grout. The failure mechanism is more complex and
94 the load resistance is difficult to predict. Dai et al. [39] conducted push-out tests and numerical
95 simulations of SHS sleeve connections for modular construction, but did not propose any analytical
96 design equations to predict grout failure. Moreover, the push-out tests may not accurately replicate real
97 loading scenarios where a connection is subjected to “pull out” and bending.

98 To address the important issues raised above, the current study designs a novel UHPFRC grouted
99 SHS tube sleeve connection, which is an improvement of the sleeve connection reported by Sui et al.
100 [19]. As the space for grouting between the outer and the inner tube is limited, using UHPFRC with
101 higher strength, higher ductility and better workability is more desirable than using normal concrete
102 with coarse aggregates. In the research reported in this paper, ten full-scale specimens under axial
103 tension are tested first to examine their failure modes and axial load resistances. The main reasons to
104 conduct axial tension tests are that not only axial tension is a potential loading scenario of the column
105 under accidental action, but also the tests will provide useful information to study flexural performance
106 of the column. Advanced 3D nonlinear FE simulation is performed then to study the stress and crack
107 development of the grouting material. Finally, a theoretical model based on the load transfer mechanism
108 observed from the tests and the FE simulations is developed to predict axial tensile resistance of the
109 UHPFRC grouted SHS tube sleeve connections.

110 **2. Full-Scale Experiment**

111 Figures 1a and 1b show the fabrication procedure of the UHPFRC grouted SHS tube sleeve connection.
112 Each column connection consists of four main parts: the upper outer tube, the lower outer tube, the
113 inner tube and the grout in the annulus. The inner tube is welded to a steel plate that is then welded to
114 the top of the lower outer tube. The connection at this region is strengthened with additional stiffeners
115 to ensure that punching shear fracture would not occur at the intersection between the inner tube and
116 the steel plate. The upper part and the lower part are then assembled on site and the annulus between
117 the inner tube and the outer tube is grouted with UHPFRC.

118 **2.1 Test specimens**

119 Figure 2 shows the configuration of the UHPFRC grouted SHS tube sleeve connection. Table 1 lists
120 the geometric parameters of the ten specimens. The main geometric parameters include the outer
121 diameter, thickness and radius of the round corner of the outer tube (B_o , t_o and r_o), the outer diameter,
122 thickness and radius of the round corner of the inner tube (B_i , t_i and r_i), the length and thickness of the
123 grout (L_g and t_g), the width and height of the shear key (w and h) and the shear key spacing (s). The
124 shear keys, in the form of steel bar of 6 mm height and 12 mm width, are welded to both the inner
125 surface of the upper outer tube and the outer surface of the inner tube, as shown in Figure 2. These
126 specimens have different shear key spacings ($s = 60$ mm, 80 mm, 120 mm), grout thicknesses ($t_g = 27$
127 mm, 32 mm, 37 mm), grout lengths ($L_g = 300$ mm, 360mm, 420 mm), and steel fiber volume ratio in
128 the UHPFRC ($V_s = 0\%$, 1%, 2%).

129 **2.2 Material properties**

130 Three types of UHPFRC with 0%, 1% and 2% steel fiber in volume are prepared for the tests. Table 2
131 shows the mix proportions of the UHPFRC that consists of type II 52.5 R Portland cement, ultrafine
132 silica fumes (SF), fine sands (grain size less than 4 mm), ground granulated blast furnace slags (GGBFS),
133 polycarboxylate superplasticizer, shrinkage-reducing admixtures and steel fibers (12 mm in length and
134 0.6mm in diameter) [19]. With added steel fibers, the compressive strength of UHPFRC-1% and
135 UHPFRC-2% tends to increase. Thus, in order to ensure that the two grout materials have similar
136 compressive strength to the UHPFRC without steel fibers (around 100 MPa), a slightly higher W/B
137 ratio of the UHPFRC-1% and UHPFRC-2% than that of the UHPC are used (Table 2). For each mixture,
138 three $\Phi 100 \times 200$ mm concrete cylinders according to ASTM C39/C39M [40] are prepared for
139 compressive strength tests, and five concrete coupons according to JSCE-2008 [41] are prepared for
140 tensile strength tests. The material properties of the concrete from the tests are summarized in Table 3.

141 It is noted that the compressive strengths of the three types of UHPFRC are around 100 MPa. In this
142 case, the connections are grouted by the UHPFRC with similar compressive strength but different steel
143 fiber contents. The SHS tubes and plates are made of mild steel Q235, and the shear keys is made of
144 HRB 400 rebar. Material coupons from the corner region of the tubes and the flat regions of both the
145 tubes and steel plates are tested, respectively. A universal test machine was used for the tensile tests of
146 the steel coupons and rebars based on ASTM E8/E8M-2016 [42]. Table 4 summarizes the Young's
147 modulus, 0.2% offset yield strength f_y , and ultimate strength f_u of the steel tubes, plates and rebars,
148 respectively.

149 **2.3 Test set-up, loading and measurement**

150 Figure 3 shows the test set-up and measurement scheme. The test adopted a computer-controlled servo
151 hydraulic actuator with a tensile capacity of 5000 kN. By using high-strength bolts, the top of the
152 specimen is connected to the ball joint of the actuator, and the bottom of the specimen is connected to
153 the bearing floor. The actuator applies an axial tensile force on the top of the specimen through
154 displacement control with a loading rate of 0.2 mm/min. The loading rate increases to 1 mm/min when
155 the specimen starts to yield or the loading force starts to drop down. The Linear Variable Displacement
156 Transducers (LVDTs), T1 and T2, measure the vertical displacement at the top of the specimen, and T3
157 and T4 measure the vertical displacement at the point of connection. It should be noted that, to measure
158 the actual deformation of the specimen and the connection, additional LVDTs have to be installed near
159 the bottom of the specimen to observe the deformation of the bottom plate. Strain gauge pairs, OH1-6
160 and OV1-6, are evenly distributed along the length of the outer tubes to measure the strains both in the
161 circumferential and the longitudinal directions. IH1-2 and IV1-2 measure the circumferential and
162 longitudinal strains on the inner surface of the inner tube near the connection.

163 2.4 Failure modes

164 Figure 4 shows two typical failure modes observed from the ten UHPFRC grouted SHS tube sleeve
165 connections under axial tension. They are (1) outer tube yielding with fractured inner tube, as shown in
166 Fig. 4(a), and (2) grout shear failure, as shown in Fig. 4(b).

167 For the specimens with high shear resistance UHPFRC grout, e.g., S80T32L420F0, the outer and
168 inner tubes govern the behavior of the specimen. Bond-slip between the upper outer and inner tubes is
169 limited. The grout is almost intact since little concrete fragments drop out from the annulus of the tubes.
170 The upper outer tube above the grouted region and the lower outer tube are all yielded. The inner tube
171 near the overlapped region also yields significantly, which is finally fractured at the peak load. The
172 specimen S80T32L420F1 is supposed to exhibit a similar failure mode to specimen S80T32L420F0,
173 since the shear resistance of S80T32L420F1 is greater than that of 80T32L420F0 due to the effect of
174 the added steel fibers. However, due to operational reasons during the assembly of specimen
175 S80T32L420F1, one of the bolts connecting the end plate to the actuator was not properly installed,
176 resulting in excessive deformation of the end plate and termination of the loading process. Thus,
177 S80T32L420F1 failed due to excessive deformation of the end plate, rather than what was expected.

178 For the specimens with UHPFRC grout that has lower shear resistance than that of the outer or
179 inner tube, e.g., S120T32L300F0 and S80T32L300F0, the grout predominately governs the behavior
180 of the specimen. No obvious yielding is observed on the outer tubes. Instead, bond-slip between the
181 upper outer tube and the inner tube becomes significant. The grout starts to crack at the peak load. The
182 final status of the grout is shown in Fig. 4(b), from which serious shear cracks and crush are observed
183 at both the flat and the corner regions of the steel tube. For other specimens, e.g., S60T32L300F0,
184 S80T32L300F1, S80T32L300F2, S80T37L300F2, S80T27L300F2 and S80T32L360F1, the failure

185 modes show a mixture of the characteristics observed from the aforementioned two typical failure
186 modes, i.e., yielding is observed on the upper outer tube above the grouted region and the lower outer
187 tube, and bond-slip exists between the upper outer tube and the inner tube. Grout crushing caused by
188 shearing occurs after reaching the peak load.

189 Figure 5 shows section view of the ten specimens obtained by waterjet cutting after being tested
190 and Figure 6 displays the detailed crack patterns in the grout of each specimen. It is noted that both)
191 S80T32L420F1 and S80T32L420F0 have failed by fracture of the inner tube with limited diagonal
192 cracks in the grout. The cracks initiate from the adjacent diagonal shear keys. If the shear resistance of
193 the grout is higher than that of the outer or inner tube, the load can be effectively transferred from the
194 upper tube to the lower one through the grout. The grout may stay relatively intact before the upper tube
195 or the lower tube reaches its ultimate strength. The final failure thus would initiate from the inner tube
196 rather than outer tube, e.g., fracture of the welded part, because the inner tube has smaller sectional size
197 compared to the outer tube. However, if the ultimate strength of the outer or inner tube is higher than
198 the shear resistance of the grout, initial cracking may occur in the grout, followed by slipping between
199 the steel tube and the grout. The force from the upper tube may induce shear damage of the grout
200 associated with bond-slip between the upper outer tube and the inner tube, while the tubes may not
201 yield, depending on the effective load that is transferred to them. Ideally, from the viewpoint of design,
202 shear resistance of the UHPFRC grout can be equal to the tensile resistance of the inner tube. The crack
203 patterns of the grout are classified into two types. The first type is diagonal line crack linking two
204 staggered shear keys on the inner surface of the outer tube and the outer surface of the inner tube,
205 respectively. The two adjacent parallel diagonal line cracks form a compression strut, through which
206 the load is transferred from the outer tube to the inner tube. Based on the geometric relationship with

207 grout thickness t_g and shear key spacing s , the angle of the compression strut α is calculated as $\tan^{-1}(0.5s/t_g)$. The second type is large-area crushing of the grout along the outer surface of the inner tube.
208
209 The development of the cracks will be discussed in Section 3.

210 **2.5 Load-displacement curves**

211 Figure 7 displays the load-displacement curves of all the ten SHS-UHPFRC grout sleeve connections,
212 where P is the external load from the actuator, and δ is the vertical displacement measured at the top
213 end-plate. All the curves exhibit a similar trend before reaching the peak load resistance. The load-
214 displacement relationship is initially linear, and then nonlinear due to grout cracking. After reaching
215 the peak load resistance, the curve drops down either due to fracture of the inner tube (e.g.,
216 S80T32L420F1 and S80T32L420F0) or due to shear crushing of the grout. The peak load resistance of
217 the specimen is positively related to the shear resistance of the grout. The specimen with the longest
218 grout length, S80T32L420F0, has the largest shear resistance of the grouted part and the peak load
219 resistance reaches 3005.2 kN. The specimen S80T32L420F1 is expected to have the same level of load
220 resistance to S80T32L420F0. However, due to the operational reasons discussed above, which causes
221 prematurely excessive deformation of the end plate, thus lower than expected load resistance. The
222 specimen with the shortest grout length and largest shear key spacing, S120T32L300F0, has the lowest
223 shear resistance of the grouted part with a peak load resistance of only 1404.6 kN. Evidently, grout
224 resistance design is of great significance in the design of the connection.

225 **2.6 Load-strain curves**

226 Figure 8 displays the load-strain curves at the measuring points. For all the specimens except
227 S120T32L300F0 and S80T32L420F0, the circumferential and longitudinal strains measured at the
228 lower outer tube (OH-3, OH-6, OV-3 and OV-6) are far beyond the yield strain of the steel, indicating

229 that the lower outer tube has yielded significantly. It is found that the circumferential strain is much
230 larger than the longitudinal one for OV3. It may be because: (1) OH3 and OV3 are located right below
231 the welded stiffener where stress concentration occurs and (2) necking or buckling near the welded
232 point has occurred, resulting in a higher strain in the circumferential in the longitudinal direction. The
233 other regions on the outer tubes also yield but with smaller yield strain (e.g., location OH-1, OH-4). For
234 S120T32L300F0, the largest strain measured at the outer tubes is close to the yield strain of the steel,
235 which indicates that the design strength of the grout part is equal to that of the steel tube. This will cause
236 simultaneous shear failure of the grout and yield of the steel tube. In this case, the strength of the grout
237 connection can be properly designed. For S80T32L420F0, the strains measured at the upper outer tube
238 above the grouted part (OH-1, OH-4, OV-1 and OV-4) and at the lower outer tube (OH-3, OH-6, OV-
239 3 and OV-6) are far greater than the yield strain of the steel, indicating both the upper outer tube and
240 the lower outer tube have yielded significantly. However, the measured strains at the outer tube within
241 the grouted part are very small. In view of the failure mode, it can be concluded that the UHPFRC
242 grouted part of S80T32L420F0 has sufficient strength to transfer fully the load from the upper tube to
243 the lower tube.

244 **2.7 Effect of shear key spacing**

245 Figures 9(a) compares the load-displacement curve and the load-longitudinal strain distribution
246 respectively, of the SHS-UHPFRC sleeve grout connections with shear key spacing of 60 mm, 80 mm
247 and 120 mm. The shear key spacing significantly affects the load resistance of the connection. The peak
248 load resistance decreases with the increase of shear key spacing since fewer number of shear keys result
249 in fewer number of compression struts formed in the grout to carry the axial force. At the peak load,
250 the longitudinal strains at the lower outer tube of the three specimens are higher than the yield strain.

251 The measured strains at the outer tube within the grouted part are lower than the yield strain, indicating
252 that the outer tube within this region is effectively strengthened by the grout and with reduced
253 deformation.

254 **2.8 Effect of grout length**

255 Figure 9(b) compares the load-displacement curve and load-longitudinal strain distribution of the
256 grouted connections with varying grout length of 300 mm, 360 mm and 420 mm, respectively. The
257 specimen S80T32L420F0 and S80T32L420F1 are designed with high strength grouted part (420 mm),
258 which are expected to fail due to yielding of the steel tube, although S80T32L420F1 fails earlier due to
259 the excessive deformation of the end plate as discussed in Section 2.4 and 2.5. It can be seen from the
260 curves that the shear resistance of the grouted part is positively related to the grout length. The specimen
261 S80T32L420F0 fails by fracture of the inner tube, while the specimen S80T32L300F1 and
262 S80T32L360F1 fail by shear crushing of the grout. The load-displacement curves show that the peak
263 load resistance increases with the increase of grout length. More shear keys exist in a longer grout,
264 which provide larger mechanical interlock strength with more compression struts to contribute to the
265 strength of the grout to sustain the axial force. Moreover, a longer grout has increased contact area
266 between concrete and steel tube, which increases the interfacial bond resistance of the grouted
267 connection.

268 **2.9 Effect of grout thickness**

269 Figure 9(c) compares the load-displacement curve and load-longitudinal strain distribution of the
270 grouted connections with varying grout thickness of 27 mm, 32 mm and 37 mm, respectively. The load-
271 displacement behavior and the peak load resistance of the three specimens are very close to each other,
272 indicating that the grout thickness has marginal effect on the load resistance of the grouted connections.

273 This is because an increase of grout thickness only changes the compression strut angle and does not
274 increase the number of shear keys and the contact area between the concrete and steel tubes. Since the
275 allowable change of grout thickness is very limited, the resulted difference in shear resistance of the
276 grout is small. For the sake of practicability, a minimum grout thickness of two fiber length, i.e., 24mm
277 in the present study, is recommended. For each specimen, the part of the outer tube outside the grouted
278 zone has all yielded. However, the grouted part is still within elastic stage. This indicates that the high
279 strength grouted connection is effective in transferring the load from the upper to the lower tube.

280 **2.10 Effect of volume fraction of steel fiber in UHPFRC**

281 Figure 9(d) compares, respectively, the load-displacement curve and load-longitudinal strain
282 distribution of the grouted connections with steel fiber volume fraction of 0%, 1% and 2%. The small
283 addition of steel fibers increases both compressive and tensile strength of the grout to some extent. The
284 design compressive strength of the three UHPFRC are 96.6 MPa, 105.8 MPa and 108.9MPa,
285 respectively, as shown in Table 3. However, the shear strength of the three mixes are significantly
286 different. The comparisons in Fig.9(d) show that the peak load resistances of S80T32L300F1 and
287 S80T32L300F2 are very close, which are much higher than that of S80T32L300F0. This is attributed
288 to enhanced shear strength of the grouted connections, S80T32L300F1 and S80T32L300F2, that are
289 significantly higher than that of S80T32L300F0. The comparisons also show that the UHPFRC with a
290 fiber volume fraction of 1% is the best shear design of the three, indicating that a higher fiber volume
291 fraction (>1%) may not be beneficial. This will also reduce the cost of UHPFRC. Moreover, as shown
292 in the loading curves in Figure 9d, a higher fiber volume fraction (2%) provides a higher peak
293 displacement. This indicates that the added fibers also improve ductility of the connection. As shown
294 in Table 3, with different fiber volume fractions, the three UHPFRC have similar tensile strength f_t ,

295 while their shear strength, f_v , are significantly different. From the above observations, it can be
296 concluded that shear resistance of the grout connections is best characterized by their respective shear
297 strength, as the tensile strength is much less sensitive to fiber fraction. Moreover, the longitudinal strains
298 at the lower outer tube of these three specimens are higher than the yield strain, leading to a full
299 utilization of material strength.

300 **3. Numerical Modelling**

301 This study also performs numerical simulation to further understand the load transfer mechanism of the
302 grouted connection and the state of stresses of the grouted connection during loading. The numerical
303 simulation is executed using the standard static solver in the advanced finite element program ABAQUS.

304 **3.1 Material model of UHPFRC and steel**

305 The material model adopts the concrete damage plasticity (CDP) model to represent the behavior of the
306 UHPC and UHPFRC. The CDP model specifies the inelastic behavior of concrete as elasticity-based
307 isotropic damage in combination with isotropic tensile and compressive plasticity. The definition of the
308 CDP model requires compressive constitutive relationship (including compressive stress-strain curve
309 and damage variables), tensile constitutive relationship (including tensile stress-strain curve and
310 damage variables), yield surface and flow potential parameters. According to the material test results,
311 the 28-day cylinder compressive strength and tensile strength of UHPC, UHPFRC (1%) and UHPFRC
312 (2%) are used to calibrate the FE model. Sui et al. [19] and Zhang et al. [43] have discussed the
313 compressive and tensile constitutive relationship for UHPFRC and UHPC, respectively, and proposed
314 the nondimensional stresses-inelastic strain curves and nondimensional damage variables-inelastic
315 strain curves, which are directly used in the current study. The yield surface and flow potential
316 parameters, including the dilation angle, second stress invariant ratio (K), ratio of biaxial to uniaxial

317 compressive strength (f_{b0}/f_{c0}), eccentricity and viscosity factor are specified as 45°, 0.667, 1.07, 0.1 and
318 0.0001, respectively. The steel section adopts the elastic-plastic model which transfers the engineering
319 stress-strain relationship to the true stress-strain relationship. Since the round corner of the SHS tube
320 hardens in the cold-forming process during fabrication, the material properties of this part are separately
321 defined.

322 **3.2 Element type, boundary condition and contact definition**

323 Figure 10 shows the FE model of the grouted connection, and only one quarter of the model is built
324 since the engineering stresses and strains of the structure are symmetric in the XZ and the YZ planes.
325 Both the steel and the concrete are meshed using the eight-node solid element with reduced integration
326 (C3D8R), which is adequate for the nonlinear analysis especially in contact simulation. **Convergence**
327 **analysis has been conducted to investigate the sensitivity of the mesh size.** The global element size for
328 the steel tubes is 8 mm and for the concrete is 4 mm. The elements around the shear keys and the corner
329 of the tubes and concrete are further refined. To simulate the real boundary conditions at the top and
330 bottom of the specimens, the through-hole bolts are modelled between the end plate and the rigid end
331 plate. In this case, the rigid bottom plate is fixed, while the top end plate is coupled with a reference
332 point, where a vertical displacement load acts. The contacts between concrete and steel, between bolts
333 and plates, and between plates adopt the standard general contact. The two contact surfaces are defined
334 by the balanced master-slave relationship to guarantee the accuracy of the contact analysis. The contact
335 properties include both normal and tangential behavior. The former is specified as hard contact, and the
336 latter is specified by a friction coefficient of 0.7 for concrete-steel contact and 0.5 for steel-steel contact.

337 **3.3 Validation of FE model**

338 Figure 11 compares the load-displacement curves of the ten grouted connections obtained from the tests
339 and the FE simulations. The FE models present good predictions of the load-displacement curves before
340 the peak load is reached for the first eight specimens. The predicted load resistance is very close to the
341 test values. When approaching the peak load, significant amount of cracks are generated in the grout.
342 The load resistance of the specimen is reduced due to shear crushing of the grout and the load-
343 displacement curves show dramatical load drops. The FE simulation terminates due to numerical
344 convergence problem caused by serious damage of concrete. For S80T32L420F0 and S80T32F420F1,
345 the load-displacement curves by FE simulation increase monotonically and this continues after the
346 failure point from the tests. This is because the grout experiences only minor damage during loading.
347 The failure of these two specimens is governed by the steel inner tube whose damage is not considered
348 in the constitutive model of the steel material. Thus, the fracture process of the inner tube is ignored in
349 the simulation. However, the predicted load-displacement curves of these specimens match very well
350 with those from the tests before the peak load resistance.

351 **3.4 Development of concrete cracks**

352 Compared to the experimental results, the validated FE model provides a convenient and useful tool to
353 extract detailed information on the development of crack in the grout. Figure 12 plots stiffness
354 degradation of the grout at two critical stages, i.e., when the load is half of the peak load and at the peak
355 load. For the first eight specimens failed by grout shear crushing, the crack pattern in the grout is initially
356 diagonal between two staggered shear keys on the inner surface of the outer tube and the outer surface
357 of the inner tube. At the peak load, the diagonal line cracks develop rapidly, leading to severe crushing
358 along the longitudinal direction and large bond-slip between grout and steel tubes. For the last two
359 specimens with larger grout length, only minor diagonal line cracks are formed and the grout is not

360 crushed. The damage of the grout at the end of test is also presented for comparisons. As can be seen
361 in Figure 12, generally, the proposed FE model is able to satisfactorily reproduce the damage in the
362 grout observed from the tests.

363 **4. Theoretical model of axial load resistance**

364 According to the test and numerical results, there are two types of failure modes when an UHPFRC
365 grouted SHS tube sleeve connection is subjected to axial tension, They are (1) inner tube fracture, and
366 (2) shear crushing of the grout associated with bond-slip between the grout and steel tube. Therefore,
367 the axial load resistance associated with the first failure mode can be obtained by multiplying the
368 ultimate strength of steel by the cross-section area of the inner tube. The second failure mode is,
369 however, more complex due to shear crushing of grout. Hence, the axial load resistance associated with
370 the second failure mode needs to be evaluated appropriately. To provide guidance for the design of
371 UHPFRC grouted SHS tube sleeve connections, this section derives a theoretical model based on the
372 load transfer mechanism of the sleeve connection to predict the axial load resistance.

373 **4.1 Existing analytical models for pile-to-sleeve connection**

374 Currently, there is not any design guideline for axial load resistance of UHPFRC grouted SHS tube
375 sleeve connections. The only relevant design guideline is for axial load resistance of pile-to-sleeve
376 connections normally used for offshore structures, such as offshore pile foundations and transition
377 pieces of wind turbine towers, etc. The main difference is that the cross sections of piles and sleeves
378 are of circular hollow section (CHS). For a pile-to-sleeve connection subjected to axial load, the
379 ultimate shear stress τ_u is defined as the ratio of ultimate axial load resistance P_u to the outer surface
380 area of the pile within the grouted region, as given in Eq.(3),

$$381 \quad \tau_u = \frac{P_u}{\pi D_p L_g} \quad (3)$$

382 where D_p is the outer diameter of the inserted pile, and L_g is the length of the grouted region.

383 The axial load resistance of pile-to-sleeve connections is developed from, firstly, the bond strength
384 due to friction and adhesion between grout and pile and, secondly, the mechanical interlock strength
385 from shear keys. Existing design codes have given different equations to predict shear stress in a pile-
386 to-sleeve connection. These equations include two terms related, respectively, to the two aspects
387 mentioned above, each of which needs to be calculated independently. Based on a large number of
388 experimental data, DNV 2014 [35] proposed the following equation for shear resistance,

$$389 \quad \tau_u = \left[\frac{800}{D_p} + 140 \left(\frac{h}{s} \right)^{0.8} \right] k^{0.6} f_{cu}^{0.3} \quad (4)$$

390 where the first term is attributed to friction and adhesion, and the second term is to mechanical
391 interlocking. h is shear key height, s is shear key spacing, f_{cu} is concrete compressive strength, and k is
392 radial stiffness parameter which is defined as:

$$393 \quad k = \left[\frac{D_p}{t_p} + \frac{D_s}{t_s} \right]^{-1} + \frac{E_g}{E_s} \left[\frac{D_s - 2t_s}{t_g} \right]^{-1} \quad (5)$$

394 In which D_s is outer diameter of the sleeve, t_p , t_s , t_g are thickness of the pile, sleeve and grout,
395 respectively. E_s and E_g are elastic modulus of the steel and concrete, respectively.

396 Based on the load transfer mechanism of pile sleeve connection, Krahl and Karsan [31] have
397 established a set of force equilibrium equations for a cracked compression strut in grout, and derived
398 shear stress due to mechanical interlock in relation to shear key height, shear key spacing and concrete
399 compressive strength. The bond strength due to friction and adhesion is determined as a constant based
400 on a regression analysis of experimental data. The ultimate shear resistance is shown as below.

$$401 \quad \tau_u = 1.15 + 1.72 f_{cu} \left(\frac{h}{s} \right) \quad (6)$$

402 To conservatively estimate axial load resistance and extend this equation to pile-to-sleeve
 403 connections without shear keys, API 2007 [37] recommended a smaller value for the coefficient of the
 404 second term, as given in Eq. (7).

$$405 \quad \tau_u = 0.138 + 0.5f_{cu} \left(\frac{h}{s} \right) \quad (7)$$

406 As the cross-section shapes of the UHPFRC grouted SHS tube sleeve connection and the CHS
 407 pile-to-sleeve connection are different, the interfacial bond strength between the concrete and steel
 408 tubes as well as the confinement to the grout are very different. Thus, the axial load resistance equations
 409 for pile-to-sleeve connection cannot be directly applied to UHPFRC grouted SHS tube sleeve
 410 connections.

411 **4.2 Friction and adhesion for UHPFRC grouted SHS tube sleeve connection**

412 The axial load resistance due to friction and adhesion for UHPFRC grouted SHS tube sleeve connection
 413 is calculated as:

$$414 \quad P_b = \tau_b \cdot 4B_i L_g \quad (8)$$

415 where τ_b is bond strength; B_i is width of the inner tube, L_g is length of the grouted region.

416 Roeder et al. [44] have investigated the factors affecting bond strength of concrete-filled steel tubes
 417 and concluded that SHS tubes possessed lower bond strength than CHS tubes. In addition, bond strength
 418 is not sensitive to concrete strength, but negatively related to tube diameter and diameter-to-thickness
 419 ratio. Based on a regression analysis of experimental data, Lyu and Han [45] derived the bond strength
 420 equations shown in Eqs.(9) and (10) for CHS and SHS concrete-filled steel tubes, respectively.

$$421 \quad \tau_{b_CHS} = 0.071 + 4900 \left(\frac{t}{D^2} \right) \quad (9)$$

$$422 \quad \tau_{b_SHS} = 0.043 + 1100 \left(\frac{t}{B^2} \right) \quad (10)$$

423 Eq. (9) and Eq. (10) have the similar form but with different coefficients. To unify the above two
 424 equations and make the bond strength equation applicable to different shapes of cross section, Eq. (11)
 425 below is proposed for grouted SHS tube connections by introducing corner radius to width ratio $2r_o/B_o$,
 426 where r_o and B_o are corner radius and width of outer tube, respectively. If $2r_o/B_o=0$, the cross section is
 427 square and Eq. (11) is reduced to Eq. (10); if $2r_o/B_o=1$, the cross section is circular and Eq. (11) becomes
 428 Eq. (9); if $0<2r_o/B_o<1$, the cross section is square with rounded corners

$$429 \quad \tau_b = \left(0.043 + 0.028 \frac{2r_o}{B_o} \right) + \left(1100 + 3800 \frac{2r_o}{B_o} \right) \left(\frac{t_o}{B_o^2} \right) \quad (11)$$

430 **4.3 Shear key interlock for UHPFRC grouted SHS tube sleeve connection**

431 The load resistance due to mechanical interlock of shear keys is calculated as below:

$$432 \quad P_s = n f_{cu}^* \cdot 4(B_i + h)h = 4 f_{cu}^* (B_i + h) \frac{h L_g}{s} \quad (12)$$

433 where $n=L_g/s$ is number of shear keys; f_{cu}^* is confined concrete strength; B_i , h , L_g and s are width of
 434 inner tube, shear key height, shear key spacing, and grout length, respectively.

435 The shear resistance contributed by shear keys is calculated by dividing the load resistance by the
 436 outer surface area of the inner tube within the grouted part. Let $\xi = f_{cu}^*/f_{cu}$, then,

$$437 \quad \tau_s = \frac{P_s}{4B_i L_g} = \xi f_{cu} \left(1 + \frac{h}{B_i} \right) \frac{h}{s} \quad (13)$$

438 For a cracked compression strut, the free body diagram is shown in Figure 13(a). The triangular
 439 part with side length of ah represents the critical region of the concrete contributing to the load
 440 resistance. Because this critical region cannot be seen during loading, the section has been cut apart
 441 after the test. Thus, the size of the triangular part can be directly extracted from the FE results or test
 442 results [31], as shown in Fig. 13(b). Table 5 lists the values of a for all the ten specimens. As these
 443 values are very close to each other, the average value of them, 3.8, is used for a in the following study.

444 Based on force and bending moment equilibrium for the free body shown in Figure 13(a), the
 445 following equations (14)-(16) can be established.

$$446 \quad 4B_1F_5 + 4(B_1 + h)F_1 = 4(B_o - 2t_o)F_6 + 4(B_o - 2t_o - h)F_2 \quad (14)$$

$$447 \quad 4B_1F_3 = 4(B_o - 2t_o)F_4 \quad (15)$$

$$448 \quad 4(B_o - 2t_o - h)F_2 \cdot (t_g - 0.5h) + 4(B_o - 2t_o)F_6 \cdot t_g = 4(B_o - 2t_o)F_4 \cdot (0.5s - ah) + 4(B_1 + h)F_1 \cdot 0.5h \quad (16)$$

449 In addition, the following relationships exist between the forces.

$$450 \quad F_1 = hf_{cu}^* \quad (17)$$

$$451 \quad F_5 = \mu F_3 \quad (18)$$

$$452 \quad F_6 = \mu F_4 \quad (19)$$

453 where μ is the friction coefficient between the steel tube and the concrete. Six unknown forces exist in
 454 the above six independent equations. In order to evaluate the confining effect, the ratio of F_3 to F_1 is
 455 solved as:

$$456 \quad R = \frac{F_3}{F_1} = \frac{(B_1 + h)(t_g - h)}{B_1(1.5s - ah - \mu t_g)} \quad (20)$$

457 F_3 is also the product of the normal confining pressure f_{conf} and the side length of the critical
 458 triangular part ah .

$$459 \quad F_3 = ahf_{conf} \quad (21)$$

460 Combining Eqs. (17), (20) and (21) yields,

$$461 \quad \frac{F_3}{F_1} = \frac{ahf_{conf}}{hf_{cu}^*} = \frac{af_{conf}}{f_{cu}^*} = R \quad (22)$$

462 The lateral confinement of the grout is affected by the corners of the column cross section [46].
 463 Wu and Wang [47] have proposed a unified strength model for square and circular concrete columns
 464 confined by fiber reinforced polymer (FRP) materials. The strength model for columns with a corner
 465 radius degenerates into a model for circular columns when the corner radius is half of the column width,

466 and degenerates into a model for sharp corner square columns when the corner radius is zero. Faustino
 467 et al. [48] has simplified the relationship between f_{cu}^* and f_{conf} , as shown in Eq. (23), by introducing
 468 $2r_o/B_o$ to consider the corner effect,

$$469 \quad f_{cu}^* = f_{cu} + k \frac{2r_o}{B_o} f_{conf} \quad (23)$$

470 where k is a constant coefficient.

471 For the UHPFRC grouted SHS tube sleeve connections, this study intends to develop a similar
 472 unified strength model considering the corner effect. Fig. 13(c) shows the confinement state of grout in
 473 the UHPFRC grouted SHS tube sleeve connection. Only the grout within the shaded area can be
 474 effectively confined for SHS. According to Krahl and Karsan [31], the confined strength of grout in the
 475 CHS pile-to-sleeve connection is determined as $f_{cu}^* = f_{cu} + 4.1f_{conf}$. Thus, the unified strength model
 476 for the grout in the UHPFRC grouted SHS tube sleeve connection with rounded corners is proposed as,

$$477 \quad f_{cu}^* = f_{cu} + 4.1 \frac{2r_o}{B_o} f_{conf} \quad (24)$$

478 Substituting Eq. (24) into Eq. (22), the ratio of f_{cu}^* to f_{cu} can be obtained,

$$479 \quad \xi = \frac{f_{cu}^*}{f_{cu}} = \frac{a}{a - 4.1 \frac{2r_o}{B_o} R} = \frac{a}{a - \frac{8.2r_o}{B_o} R} \quad (25)$$

480 Substituting Eq. (25) into Eq. (13), the shear resistance due to mechanical interlock of shear keys
 481 can be determined by Eq.(26),

$$482 \quad \tau_s = \left(1 + \frac{h}{B_i}\right) \frac{h}{s} \frac{a}{a - \frac{8.2r_o}{B_o} R} f_{cu} \quad (26)$$

483 where a has been determined from the FE model as shown in Table 5 and R is calculated by Eq. (20).

484 **4.4 Prediction of axial load resistance**

485 Similar to CHS pile-to-sleeve connections, axial load resistance of UHPFRC grouted SHS tube sleeve
 486 connections consists of the bond strength due to friction and adhesion between grout and steel tubes

487 and the mechanical interlock due to shear keys. Based on the discussions in Sections 4.2 and 4.3, the
 488 total shear stress is calculated as,

$$489 \quad \tau_u = \tau_b + \tau_s = \left[\left(0.043 + 0.028 \frac{2r_o}{B_o} \right) + \left(1100 + 3800 \frac{2r_o}{B_o} \right) \left(\frac{t_o}{B_o^2} \right) \right] + \left[\left(1 + \frac{h}{B_i} \right) \frac{h}{s} \frac{a}{a - \frac{8.2r_o}{B_o} R} f_{cu} \right] \quad (27)$$

490 The axial load resistance is then obtained by multiplying the shear stress with the cross-sectional
 491 area of the inner tube within the grouted region as follows.

$$492 \quad P_u = 4B_i L_g \tau_u \quad (28)$$

493 **4.5 Validation of theoretical model**

494 The proposed model for the axial load resistance of an UHPFRC grouted SHS tube sleeve connection
 495 is validated against the test results of the ten specimens in this study and the four specimens tested
 496 independently by Dai et al. [39]. Table 6 lists the calculated shear stresses and load resistances of these
 497 specimens as well as the comparisons between the predicted axial load resistance and the test results. It
 498 can be seen that the axial load resistance due to friction and adhesion contributes less than 10% of the
 499 total axial load resistance. The main contribution of the load axial resistance is the mechanical interlock
 500 of the shear keys which provides over 90% of the total resistance. As can be seen, the calculated total
 501 axial load resistances of the UHPFRC grouted SHS tube sleeve connections are reasonably close to the
 502 test results. Figure 14 plots the ratios of the test results to the predicted results. The mean value of the
 503 ratios is 1.21 with a standard deviation of 0.17. Thus, the proposed theoretical model is reasonably
 504 successful in predicting axial load resistance of the UHPFRC grouted SHS tube sleeve connections
 505 failed by grout shear crushing associated with bond-slip between the grout and steel tube. The
 506 predictions are relatively conservative, which is beneficial for practical design.

507 **5. Conclusion**

508 An novel UHPFRC grouted SHS tube sleeve connection has been developed and its axial load resistance
509 behavior has been investigated experimentally, numerically and theoretically. The experimental
510 program tested ten full-scale sleeve connection specimens with different shear key spacings, grout
511 thicknesses, grout lengths and volume proportions of steel fibers in the UHPFRC. An advanced FE
512 model was built for the UHPFRC grouted SHS tube sleeve connection to examine its load-displacement
513 curve behavior, stress and strain development as well as crack development of the grout. Based on the
514 load transfer mechanism, a theoretical model was developed to predict axial load resistance of the
515 UHPFRC grouted SHS tube sleeve connections subjected to tension. The researched reported in the
516 paper supports the following conclusions:

- 517 (1) There are two types of failure modes, namely, (a) inner tube fracture, and (b) grout shear crushing
518 associated with bond-slip between grout and steel tube, when an UHPFRC grouted SHS tube sleeve
519 connection is subjected to axial tension. For a grouted sleeve connection with high strength
520 grouted part, failure of the connection is governed by fracture of the inner tube. While for the
521 grouted sleeve connection of lower shear resistance, failure is governed by the shear in the grout.
- 522 (2) For shear crushing failure of the grout, the FE simulation can successfully reproduces cracks
523 development in the grout. During loading, diagonal line cracks initially appear between staggered
524 shear keys on the inner surface of the outer tube and the outer surface of the inner tube. At the peak
525 load, the diagonal line cracks develop rapidly causing severe concrete crushing along the tube
526 surface, resulting in large bond-slip between the concrete and steel tubes.
- 527 (3) The axial load resistance of an UHPFRC grouted SHS tube sleeve connection decreases with shear
528 key spacing but increases with grout length. Grout thickness has marginal effect on the load
529 resistance of the grouted connection. The addition of steel fiber up to 1% in volume is effective in

530 increasing load resistance of the grouted sleeve connection. A higher fiber volume addition (>1%
531 in volume) is not necessarily beneficial in design because it may not further enhance the shear
532 resistance of the grouted sleeve connection.

533 (4) The newly derived theoretical formula in this paper is effective in predicting tensile resistance of
534 the grouted connection. Corner radii factors are considered in the new model to consider the effect
535 of sectional shape on the bond strength between grout and steel tube, and the confinement of the
536 grout. The load axial resistance equation consists of two terms, namely, the friction and adhesion
537 between grout and steel tubes, and the mechanical interlock contribution by shear keys.

538 (5) The new formula provides effective predictions to axial load resistance of UHPFRC grouted SHS
539 tube sleeve connections subjected to tension. The validation against the test data in this paper and
540 published literature indicates that the new formula can provide reasonably reliable and accurate
541 prediction to axial load resistance for design purposes.


542 (6) The present study mainly focuses on the axial load resistance of the novel UHPFRC grouted SHS
543 tube sleeve connection. In the real practice, the connection in a modular construction may be
544 subjected to complex state of stresses, e.g., dead load along with seismic or wind load. Thus,
545 future research to conduct studies on flexural, shear and hysteretic behavior of the grouted SHS
546 tube sleeve connection subjected to combined bending, shearing and seismic loading is required to
547 ensure better and deeper understanding of the new grouted sleeve connection.

548 Acknowledgement

549 The authors would like to acknowledge the research grant received from the National Natural Science
550 Foundation of China (Grants No. 51978407), Shenzhen Basic Research Project (Grant No.
551

552 JCYJ20180305124106675), and Guangdong Provincial Key Laboratory of Durability for Marine Civil
 553 Engineering (SZU) (Grant No. 2020B1212060074).

Nomenclature

ah	Side length of the critical triangle in the grout under the shear key
h	Shear key height
f_{conf}	Normal confining pressure
f_{cu}	Compressive strength of concrete
f_{cu}^*	Confined concrete strength
f_t	Tensile strength of concrete
r_o, r_i	Radius of the round corner of the outer tube and the inner tube, respectively
	Shear key spacing
t_o, t_i	Thickness of the outer tube and the inner tube, respectively
w	Shear key width
B_o, B_i	Width of the outer tube and the inner tube, respectively
E_c	Elastic modulus of concrete
E_s	Elastic modulus of steel
L_g	Length of the grouted region
P_b	Load resistance due to friction and adhesion
P_s	Load resistance due to mechanical interlock of shear key
P_u	Ultimate axial load resistance
T_g	Thickness of the infilled grout
V_s	Volume proportion of steel fiber
τ_b	Shear stress due to friction and adhesion
τ_s	Shear stress due to mechanical interlock of shear key
τ_u	Ultimate shear stress
ξ	Ratio of f_{cu}^* to f_{cu}
μ	Friction coefficient between concrete and steel

554 **Data Availability Statement**

555 All data, models, and code generated or used during the study appear in the submitted article.

556 **References**

- 557 [1] Lawson M, Ogden R, Goodier C. Design in modular construction[M]. CRC Press, 2014.
- 558 [2] Mills S, Grove D, Egan M. Breaking the pre-fabricated ceiling: challenging the limits for modular high-rise.
559 2015 New York Conference Proceedings, CTBUH. 2015: 416-425.
- 560 [3] Generalova E M, Generalov V P, Kuznetsova A A. Modular buildings in modern construction[J]. Procedia
561 engineering, 2016, 153: 167-172.
- 562 [4] Liew J Y R, Chua Y S, Dai Z. Steel concrete composite systems for modular construction of high-rise buildings.
563 Structures. Elsevier, 2019, 21: 135-149.
- 564 [5] Gao S, Low S P, Nair K. Design for manufacturing and assembly (DfMA): a preliminary study of factors
565 influencing its adoption in Singapore. Architectural engineering and design management, 2018, 14(6): 440-456.
- 566 [6] Lawson R M, Ogden R G, Bergin R. Application of modular construction in high-rise buildings[J]. Journal of
567 architectural engineering, 2012, 18(2): 148-154.
- 568 [7] Liu W Q, Hwang B G, Shan M, et al. Prefabricated Prefinished Volumetric Construction: Key Constraints and
569 Mitigation Strategies. IOP Conference Series: Earth and Environmental Science. IOP Publishing, 2019, 385(1):
570 012001.
- 571 [8] Pang S D, Liew J Y R, Dai Z, et al. Prefabricated Prefinished Volumetric Construction Joining Techniques
572 Review. Modular and Offsite Construction (MOC) Summit Proceedings, 2016.
- 573 [9] Liew J Y R, Dai Z, Wang Y. Prefabricated prefinished volumetric construction in high-rise buildings. 11th
574 pacific structural steel, 2016: 223-230.
- 575 [10] Liu X C, He X N, Wang H X, et al. Compression-bend-shearing performance of column-to-column bolted-
576 flange connections in prefabricated multi-high-rise steel structures. Engineering Structures, 2018, 160: 439-460.
- 577 [11] Chen Z, Liu J, Yu Y. Experimental study on interior connections in modular steel buildings. Engineering
578 Structures, 2017, 147: 625-638.
- 579 [12] Torbaghan M K, Sohrabi M R, Kazemi H H. Investigating the behavior of specially prefabricated steel
580 moment connection under cyclic loading. Adv Steel Constr, 2018, 14(3): 412-423.
- 581 [13] Lawson R M, Richards J. Modular design for high-rise buildings. Proceedings of the institution of civil
582 engineers-structures and buildings, 2010, 163(3): 151-164.
- 583 [14] Lawson R M, Ogden R G, Bergin R. Application of modular construction in high-rise buildings[J]. Journal
584 of architectural engineering, 2012, 18(2): 148-154.
- 585 [15] Li G Q, Liu K, Wang Y B, et al. Moment resistance of blind-bolted SHS column splice joint subjected to
586 eccentric compression. Thin-Walled Structures, 2019, 141: 184-193.
- 587 [16] Singapore Building Construction Authority (BCA). Design for Manufacturing and Assembly (DfMA):
588 Prefabricated Prefinished Volumetric Construction. 2017.

- 589 [17] Deng E F, Yan J B, Ding Y, et al. Analytical and numerical studies on steel columns with novel connections
590 in modular construction. *International Journal of Steel Structures*, 2017, 17(4): 1613-1626.
- 591 [18] Sanches R, Mercan O, Roberts B. Experimental investigations of vertical post-tensioned connection for
592 modular steel structures[J]. *Engineering Structures*, 2018, 175: 776-789.
- 593 [19] Sui L, Fan S, Huang Z, et al. Load transfer mechanism of an unwelded, unbolted, grouted connection for
594 prefabricated square tubular columns under axial loads. *Engineering Structures*, 2020, 222: 111088.
- 595 [20] Lotsberg I, Serednicki A, Cramer E, et al. On the structural capacity of grouted connections in offshore
596 structures. *International Conference on Offshore Mechanics and Arctic Engineering*. 2011, 44359: 667-677.
- 597 [21] Lotsberg I, Serednicki A, Lervik A, et al. Design of grouted connections for monopile offshore structures:
598 results from two joint industry projects. *Stahlbau*, 2012, 81(9): 695-704.
- 599 [22] Solland G, Johansen A. Design recommendations for grouted pile sleeve connections. *Marine Structures*,
600 2018, 60: 1-14.
- 601 [23] Dallyn P, El-Hamalawi A, Palmeri A, et al. Experimental testing of grouted connections for offshore
602 substructures: A critical review[C]//*Structures*. Elsevier, 2015, 3: 90-108.
- 603 [24] Lamport W B, Jirsa J O, Yura J A. Strength and behavior of grouted pile-to-sleeve connections. *Journal of*
604 *Structural Engineering*, 1991, 117(8): 2477-2498.
- 605 [25] Chen T, Fang Q, Zhang CH, et al. Mechanical behavior of grouted connections under compression-bending
606 loads. *Thin-Walled Structures*, 2020, 157: 107110.
- 607 [26] Billington C J, Lewis G H G. The strength of large diameter grouted connections. *Offshore Technology*
608 *Conference*. *Offshore Technology Conference*, 1978.
- 609 [27] Johansen A, Solland G, Lervik A, et al. Testing of jacket pile sleeve grouted connections exposed to variable
610 axial loads. *Marine Structures*, 2018, 58: 254-277.
- 611 [28] Wang T, Xu H, Yu M, et al. Experimental investigation on the failure modes of grouted sleeve connections
612 under thermal and mechanical loads. *Engineering Failure Analysis*, 2020, 109: 104246.
- 613 [29] Zhao X L, Ghojel J, Grundy P, et al. Behaviour of grouted sleeve connections at elevated temperatures. *Thin-*
614 *walled structures*, 2006, 44(7): 751-758.
- 615 [30] Chen T, Xia Z, Wang X, et al. Experimental study on grouted connections under static lateral loading with
616 various axial load ratios. *Engineering Structures*, 2018, 176: 801-811.
- 617 [31] Krahl N W, Karsan D I. Axial strength of grouted pile-to-sleeve connections. *Journal of Structural*
618 *Engineering*, 1985, 111(4): 889-905.
- 619 [32] Lee J H, Won D H, Jeong Y J, et al. Interfacial shear behavior of a high-strength pile to sleeve grouted
620 connection. *Engineering Structures*, 2017, 151: 704-723.
- 621 [33] Chen T, Cao C, Zhang C, et al. Numerical modeling and parametric analysis of grouted connections under
622 axial loading[J]. *Thin-Walled Structures*, 2020, 154: 106880.
- 623 [34] Lotsberg I. Structural mechanics for design of grouted connections in monopile wind turbine structures.
624 *Marine Structures*, 2013, 32: 113-135.

- 625 [35] DNV. DNV-OS-, J101 Design of Offshore Wind Turbine Structures, May 2014, 212–4.
- 626 [36] NORSOK. Design of Steel Structures Annex K-Special Design Provisions for Jackets, 2012.
- 627 [37] API RP2A-WSD. Recommended practice for planning, designing and constructing fixed offshore platforms–
628 working stress design. American Petroleum Institute, Washington DC, 2007.
- 629 [38] ISO 19902. Petroleum and Natural Gas Industries-Fixed Steel Offshore Structures, 2007.
- 630 [39] Dai Z, Dai Pang S, Liew J Y R. Axial load resistance of grouted sleeve connection for modular construction.
631 Thin-Walled Structures, 2020, 154: 106883.
- 632 [40] ASTM C39/C39M. Standard Test Method for Compressive Strength of Cylindrical Concrete Specimens,
633 West Conshohocken, PA, USA; 2014.
- 634 [41] Concrete Committee JSCE. Recommendations for Design and Construction of High Performance Fiber
635 Reinforced Cement Composites with Multiple Fine Cracks (HPFRCC), Japan; 2008.
- 636 [42] ASTM E8/E8M - 15a. Standard Test Methods for Tension Testing of Metallic Materials1, West
637 Conshohocken, 568 PA, USA; 2016.
- 638 [43] Zhang W, Choo Y S, Feng L, et al. Representation of nonlinear behavior of fully grouted K joints in pushover
639 analysis. Journal of Constructional Steel Research, 2020, 169: 106024.
- 640 [44] Roeder C W, Cameron B, Brown C B. Composite action in concrete filled tubes. Journal of structural
641 engineering, 1999, 125(5): 477-484.
- 642 [45] Lyu W Q, Han L H. Investigation on bond strength between recycled aggregate concrete (RAC) and steel
643 tube in RAC-filled steel tubes. Journal of Constructional Steel Research, 2019, 155: 438-459.
- 644 [46] Wang L M, Wu Y F. Effect of corner radius on the performance of CFRP-confined square concrete columns:
645 Test. Engineering structures, 2008, 30(2): 493-505.
- 646 [47] Wu Y F, Wang L M. Unified strength model for square and circular concrete columns confined by external
647 jacket. Journal of Structural Engineering, 2009, 135(3): 253-261.
- 648 [48] Faustino P, Chastre C, Paula R. Design model for square RC columns under compression confined with
649 CFRP. Composites Part B: Engineering, 2014, 57: 187-198.
- 650

651

Table 1: Geometric dimensions of test specimens

Specimen	$B_o \times t_o \times r_o$ (mm×mm×mm)	$B_i \times t_i \times r_i$ (mm×mm×mm)	h (mm)	w (mm)	s (mm)	T_g (mm)	L_g (mm)	V_s (%)	h/s	B_i/B_o
S80T32L300F0	250×8×30	170×12×25	6	12	80	32	300	0	0.075	0.68
S60T32L300F0	250×8×30	170×12×25	6	12	60	32	300	0	0.100	0.68
S120T32L300F0	250×8×30	170×12×25	6	12	120	32	300	0	0.050	0.68
S80T32L300F1	250×8×30	170×12×25	6	12	80	32	300	1	0.075	0.68
S80T32L300F2	250×8×30	170×12×25	6	12	80	32	300	2	0.075	0.68
S80T37L300F2	250×8×30	160×12×25	6	12	80	37	300	2	0.075	0.64
S80T27L300F2	250×8×30	180×12×25	6	12	80	27	300	2	0.075	0.72
S80T32L360F1	250×8×30	170×12×25	6	12	80	32	360	1	0.075	0.68
S80T32L420F1	250×8×30	170×12×25	6	12	80	32	420	1	0.075	0.68
S80T32L420F0	250×8×30	170×12×25	6	12	80	32	420	0	0.075	0.68

652

653

654

Table 2: Mix proportion of UHPFRC (kg/m³)

Mix	W/B	W	OPC	SF	GGBFS	S	F	HWRA	SRA
UHPC	0.19	209.5	823.3	135.5	170.1	1060.0	0	7.29	6.29
UHPFRC-1%	0.21	213.9	750.0	130.5	165.1	1120.0	78.0	7.15	6.42
UHPFRC -2%	0.24	229.1	705.0	120.5	155.1	1150.0	156.0	5.81	6.87

655

Notes: W/B=water to binder ratio; W=water; OPC=ordinary Portland cement; SF=silica fume; GGBFS= ground granulated

656

blast furnace slag; S=sand; F=steel fiber; HWRA=high Water reducing agent; SRA=shrinkage reducing agent.

657

658

Table 3: Material properties of the concrete

Concrete	f_{cu} (MPa)	E_c (GPa)	f_t (MPa)	f_c (MPa)	Poisson's ratio
UHPC	96.6	41.4	5.4	7.1	0.185
UHPFRC-1%	105.8	42.6	6.0	14.2	0.182
UHPFRC-2%	108.9	44.2	6.1	16.2	0.192

659

660

661

Table 4: Material properties of the steel components

Component	Material	E_s (GPa)	f_y (MPa)	f_u (MPa)
Inner tube flat	Mild steel	205.3	260.5	405.6
Inner tube corner	Mild steel	202.2	482.5	522.1
Outer tube flat	Mild steel	202.1	323.5	457.7
Outer tube corner	Mild steel	208.4	461.7	541.6
Steel plate	Mild steel	206.2	377.6	546.8
Shear key	HRB 400Φ6	193.6	357.0	485.0

662

663

664

Table 5: Determination of the coefficient a

Specimen	a
S80T32L300F0	3.8
S60T32L300F0	3.7
S120T32L300F0	3.9
S80T32L300F1	3.7
S80T32L300F2	3.8
S80T37L300F2	3.7
S80T27L300F2	3.8
S80T32L360F1	3.8
S80T32L420F1	3.8
S80T32L420F0	3.8
Average	3.8

665

666

Table 6: Validation of the model

Literature	Specimen	R	ξ	f_{cu} (MPa)	f_{cu}^* (MPa)	τ_b (MPa)	τ_s (MPa)	P_b (kN)	P_s (kN)	P_u (kN)	P_{test} (kN)	$\frac{P_b}{P_u}$	$\frac{P_s}{P_u}$	$\frac{P_{test}}{P_u}$
This paper	S80T32L300F0	0.36	1.10	96.6	106.5	0.31	8.27	62.7	1687.4	1750.1	1885.3	4%	96%	1.08
	S60T32L300F0	0.60	1.18	96.6	114.4	0.31	11.84	62.7	2416.1	2478.8	2133.4	3%	97%	0.86
	S120T32L300F0	0.19	1.05	96.6	101.9	0.31	5.27	62.7	1075.7	1138.4	1404.6	6%	94%	1.23
	S80T32L300F1	0.35	1.10	105.8	116.7	0.31	9.06	62.7	1848.1	1910.8	2450.5	3%	97%	1.28
	S80T32L300F2	0.35	1.10	108.9	120.1	0.31	9.32	62.7	1902.2	1964.9	2458.5	3%	97%	1.25
	S80T37L300F2	0.46	1.14	108.9	124.0	0.31	9.65	59.0	1852.6	1911.6	2515.7	3%	97%	1.32
	S80T27L300F2	0.27	1.08	108.9	117.3	0.31	9.09	66.4	1963.9	2030.3	2476.4	3%	97%	1.22
	S80T32L360F1	0.35	1.10	105.8	116.7	0.31	9.06	75.2	2217.7	2292.9	2904.3	3%	97%	1.27
	S80T32L420F1	0.35	1.10	105.8	116.7	0.31	9.06	87.8	2587.3	2675.1	2670.6	3%	97%	1.00
	S80T32L420F0	0.35	1.10	96.6	106.5	0.31	8.27	87.8	2362.3	2450.1	3005.2	4%	96%	1.23
Dai et al. [39]	S6G28	0.93	1.34	90.4	121.1	0.67	10.91	85.8	1406.5	1492.2	1645.0	6%	94%	1.10
	S4G28	0.43	1.14	90.4	103.3	0.67	6.33	86.0	818.2	904.2	1287.0	10%	90%	1.42
	S6G18	0.41	1.12	90.4	101.6	0.67	9.16	101.1	1391.9	1493.0	1728.0	7%	93%	1.16
	S4G18	0.21	1.06	90.4	96.0	0.67	5.77	101.4	880.0	981.4	1520.0	10%	90%	1.55
Mean														1.21
Std.dev														0.17